# Single-Molecule Measurements of the Impact of Lipid Phase Behavior on Anchor Strengths

**Julie A. Wieland, Andrew A. Gewirth,* and Deborah E. Leckband***

*Department of Chemistry, Department of Chemical and Biomolecular Engineering, and Fredrick Seitz Materials Research Laboratory, University of Illinois at Urbana-Champaign, Urbana, Illinois 61801*

*Received: October 5, 2004; In Final Form: December 13, 2004*

This work describes atomic force microscopy studies of the physical parameters determining the strength of lipid anchorage in bilayers as a function of the phase state of the lipid matrix. These investigations used biotinylated lipids and streptavidin-derivatized tips to quantify the lipid pullout force from different lipid matrices. Analysis of the data using both dynamic force spectroscopy and full microscopic models show that the anchorage strength is greater in gel-phase relative to fluid-phase lipids. Additional model parameter estimates provide further insights into the hidden energy barriers that determine the mechanical integrity of lipid anchors in biological membranes.

## I. Introduction

Lipid membranes provide both mechanical and barrier properties to the cell. The phospholipids that comprise the membrane are essential to the structure of the cell's surface and contain many membrane-bound constituents, including proteins, glycolipids, and glycoproteins. These components aid in several important cell functions such as membrane trafficking, cell sorting, and migration.[2,23] Their ability to perform these functions depends on the mechanical integrity of the membrane in which they are embedded. Cells undergo many environmental changes, such as changes in temperature, pH, degree of hydration, and ionic concentration, which can vary the structure and composition of the lipid membrane.[5,22] These changes can alter the membrane properties, leading to changes in membrane protein function or to such processes as bilayer fusion. The strength with which lipids are anchored in the membrane can vary depending on membrane composition.

Methods used to investigate lipid anchorage strength include the biomembrane force probe (BFP),[8] steered molecular dynamics (SMD) simulations,[20] and the surface force apparatus (SFA).[17] These techniques use either lipid vesicles or supported lipid membranes to obtain information about the lipid anchorage strength before and after a particular structural modification of the lipid.

BFP measurements utilize the micropipet aspiration technique to hold a modified 1-stearoyl-2-oleoyl-*sn*-glycero-3-phosphocholine (SOPC) vesicle in place as a single biotinylated 1,2-distearoyl-*sn*-glycero-3-phosphoethanolamine (DSPE) lipid was extracted from the vesicle membrane with a streptavidin-coated probe. In this case, two energy barriers were observed with bond rupture distances of 0.7 and 1.2 nm. These correlated nicely with both the position of a double bond located in the hydrocarbon chain of the lipid and the lipid layer thickness.[8]

In the SMD simulations, a single 1,2-dipalmitoyl-*sn*-glycero-3-phosphocholine (DPPC) molecule was extracted from a lipid layer in the liquid crystalline phase. In the simulations, the lipids were pulled out individually without the extraction of neighboring molecules. Upon the initial application of force, the lipid rearranged into a fully extended configuration, usually occurring during the first 0.5 nm of the extraction, and then pulled free from the membrane. Here, the computed extraction distance at rupture depended on the rate of pulling, increasing from ∼1.7 to 2.3 nm as the simulated pulling rates decreased. Simulated rate studies were performed at fast (0.05, 0.02 nm/ps), medium (0.01, 0.005 nm/ps), and slow (0.002, 0.001, 0.0002 nm/ps) rates.[20]

The SFA experiments measured the force between two opposing biotinylated membrane surfaces. Streptavidin was bound to one of the surfaces and then formed bonds with biotin on the opposing membrane. While exquisite precision in force loading is possible from this technique, it also provides an ensemble average of events only. Indeed, the effects observed in this paper were interpreted in terms of changes in lateral mobility of lipids affecting the number of contacts made.[17]

Single-molecule force measurements using the atomic force microscope (AFM) represent another method available to interrogate lipid anchorage strength.[4,14,15,24,29,33] This method has the advantage of utilizing a planar supported substrate and is somewhat simpler to perform than those utilizing the BFP apparatus.

This paper describes a single-molecule study comparing the strength of a lipid anchorage in a fluid versus gel lipid layers. We examine the effect of temperature on the strength of lipid anchorage within a 1,2-dimyristoyl-*sn*-glycero-3-phosphocholine (DMPC) monolayer. Lipid layers undergo a gel-to-liquid-crystalline phase transition at the chain melting temperature $T_m$. Below this temperature, the lipid layer is in a compact gel configuration with restricted rotational bond movements, increased van der Waals contacts, and decreased lateral mobility.[5,22] Above $T_m$, the lipids are in a fluid, liquid-crystalline state. DMPC was chosen for this investigation, because its $T_m$ at 24 °C[25] allows easy access to both the gel and fluid phases. It is also a lipid commonly found in the membranes of cells.[27] These measurements are similar to those performed with BFP in that single-molecule measurements of lipid anchorage strength are observed. The major difference here is that we induced structural

* To whom correspondence should be addressed. E-mail: agewirth@uiuc.edu. Phone: 217-333-8329. Fax: 217-333-2685 (A.A.G.). E-mail: leckband@uiuc.edu. Phone: 217-333-5076. Fax: 217-333-5052 (D.E.L.).

10.1021/jp045461b CCC: $30.25 
Published on Web 03/04/2005

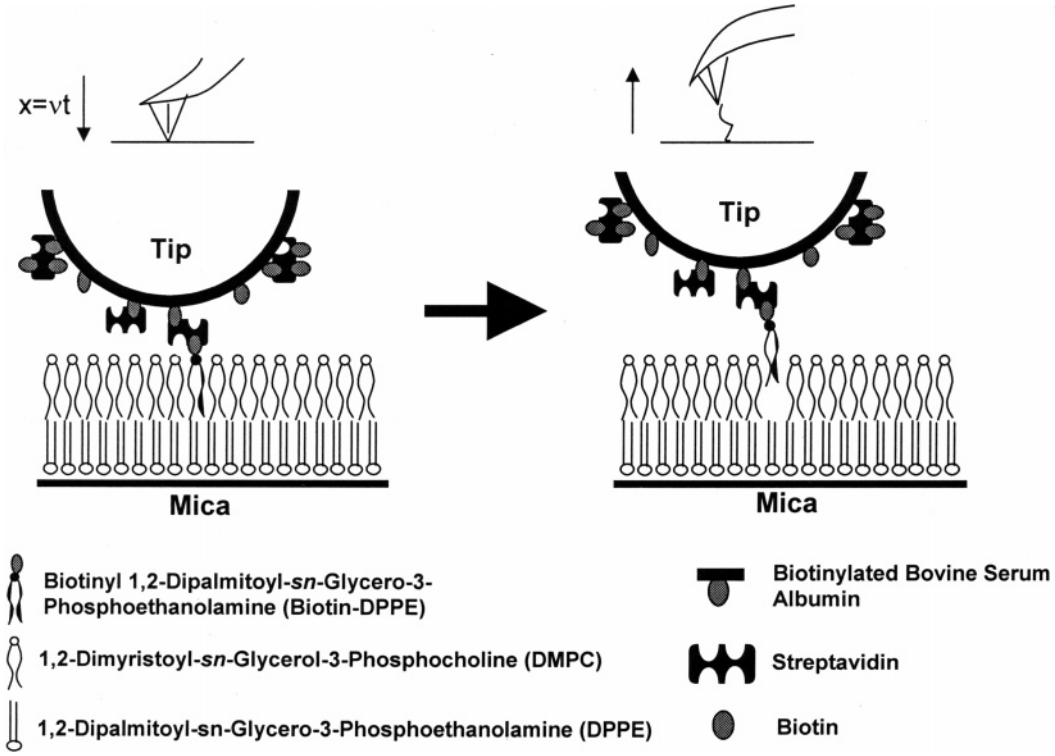


**Figure 1.** Schematic of the lipid pullout experiment.

changes in the membrane by varying temperature, whereas the BFP work used cholesterol addition to affect membrane rigidity.

We used an AFM with a temperature-controlled stage to investigate the anchorage strength of biotinyl 1,2-dipalmitoyl-*sn*-glycero-3-phosphoethanolamine (biotin-DPPE) lipids in the DMPC monolayer. A modified cantilever, sparsely coated with streptavidin, was used to extract the biotin-DPPE from its equilibrium position within the lipid layer. Because the dynamic strength of the streptavidin−biotin bond is much greater than the strengths of the lipid anchors measured thus far,[17] it is a reasonable assumption that this system could be used to test the lipid anchoring strength.

We systematically applied an external force to the bound streptavidin−biotin lipid complex by retracting the cantilever tip from the surface at various rates. This allows investigation of the bond's response to a time-dependent force and provides valuable information regarding hidden energy barriers along the bond's energy landscape. Both the dynamic force spectroscopy (DFS) analysis of Evans[6,7] and the full microscopic theory (FMT) of Szabo and Hummer[10] are used to analyze the results in this paper. These data also show that the lipid extraction force from two very similar fluid-phase lipid layers, DMPC and 1,2-ditridecanoyl-*sn*-glycero-3-phosphocholine (DTPC), which differ by only a single carbon in the alkane tails, is comparable.

## II. Materials and Methods

Figure 1 is a schematic of the lipid extraction measurement. A tip sparsely decorated with strepavidin partially biotin-blocked interacts with a biotinylated DPPE lipid diluted (1:20) in a DMPC leaflet above a DPPE leaflet, all supported on a mica surface. DPPE was chosen for the bottom leaflet, because it is always in gel phase at the temperatures utilized in these measurements. This eliminates possible complications arising from putative leaflet mixing, which can occur when both are in the fluid phase. Occasionally, the steptavidin on the tip interacts with the biotinylated lipid, leading to an interaction measured in the force curve.

**2.1. Functionalization of AFM Cantilevers.** Commercial $Si_3N_4$ V-shaped contact cantilevers with gold reflective coating (Digital Instruments, Sunnyvale, CA) were first cleaned by placing them in chloroform (Fischer Scientific) for 10 min. Tips were dried with argon and soaked in a piranha solution consisting of a 70:30 v/v mixture of concentrated $H_2SO_4$ (Mallinckrodt) and 30% $H_2O_2$ (Fisher Scientific) for 30 min. Tips were washed with Milli-Q water (Millipore, Bedford, MA), dried with argon, and placed immediately into a solution containing 0.5 mg/mL biotinylated bovine serum albumin (BBSA, Pierce Chemical, Rockford, IL). The aqueous buffer used as the solvent for this and the following solutions contained 50 mM $NaH_2PO_4$ (Fischer Scientific), 100 mM NaCl (J. T. Baker Chemical Company), and 1 mM EDTA (Fischer Scientific) and was brought to pH 7.4 by adding 1 M NaOH (Fisher Scientific). The tips were incubated in the BBSA solution for ~18 h at room temperature. The tips were rinsed with the phosphate buffer and placed in a 1-$\mu$M streptavidin (Pierce Chemical, Rockford, IL) solution for 30 min at room temperature. Tips were washed with phosphate buffer and placed in a 1.0-mg/mL solution of biotin (Sigma) for 2 h. The tips were washed with and stored in phosphate buffer until use later the same day. Spring constants were determined using the thermal fluctuations method.[11] Spring constants ranged from 0.028 N/m to 0.035 N/m.

**2.2. Surface Preparation.** Figure 2 shows the chemical structures of the lipids used in this experiment. Langmuir−Blodgett (LB) films were prepared using a commercial Langmuir−Blodgett trough (NIMA Technologies, type 611, Coventry, England) and freshly cleaved grade-V2 ruby muscovite mica. Depositions were carried out at room temperature using Milli-Q water, as described previously.[19,16,30] All lipid mixtures were prepared using a 9:1 chloroform/methanol solution (Fisher Scientific). The inner LB layer consisted of gel-phase DPPE (Avanti Polar Lipids), while the outer layer consisted of a mixture of 1:20 (molar fraction) biotin-DPPE (Avanti Polar Lipids) and DMPC (Avanti Polar Lipids), respectively. Both

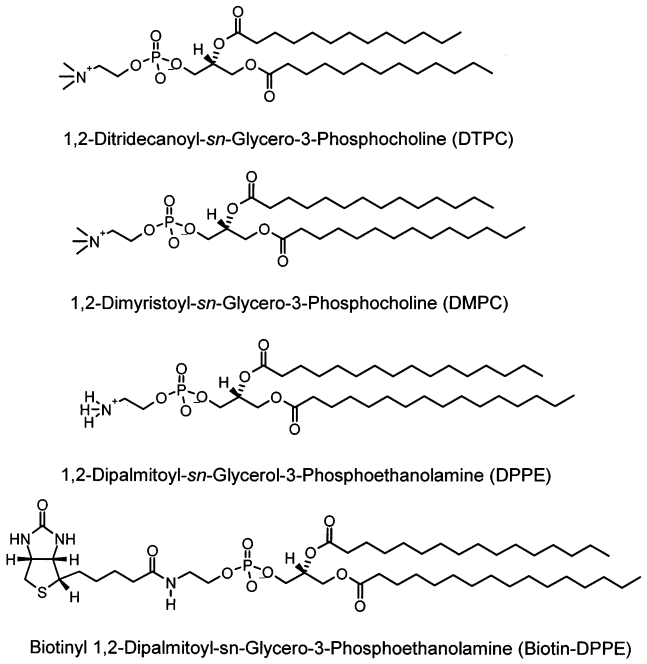


**Figure 2.** Chemical structures of DTPC, DMPC, DPPE, and biotinylated DPPE.

layers were maintained at a pressure of 37 mN/m during transfer, which corresponds to lipid densities of 0.43 $nm^2$/lipid and 0.65 $nm^2$/lipid for the inner and outer layers, respectively. The lipid-modified mica surface, maintained under solution at all times, was then transferred to the AFM cell, and phosphate buffer was exchanged with the water from the LB trough.

**2.3. AFM Setup.** All force probe measurements were obtained using a commercial AFM apparatus (Pico AFM, Molecular Imaging) with a commercial controller and data acquisition electronics (Digital Instruments). Temperatures were maintained at 30 ± 2 °C for experiments involving the fluid-phase DMPC and 15 ± 2 °C for those involving liquid-crystalline-phase DMPC. All fluid-phase DTPC measurements were performed at room temperature. Temperatures were maintained by use of a commercial temperature stage (Molecular Imaging) and a home-built temperature controller. Loading rates ranged from approximately 150−6500 pN/s (1−215 nm/s) with 1000 force extension curves obtained per loading rate. The loading rates were calculated by multiplying the tip velocity (frequency times distance traveled per cycle) by the slope of the force−distance curve just prior to bond rupture. The binding frequency (the percent of force curves generated that actually resulted in bond formation) ranged from 10% to 25%, suggesting that the population of unoccupied streptavidin binding sites was sufficiently sparse. The AFM cell was translated after every 250 measurements, to sample a new area and thereby avoid possible data bias due to wear on the substrate. Initially when the tip contacted the surface, a steady observation of bond ruptures was seen; however, this number tailed off because of depletion of the biotinylated lipid molecules from the lipid layer. The tip was moved to a new area, and the frequency of binding events increased but then decreased again after a short period of time. Tips could only be used for about 1000 force measurements before binding sites on the tip became saturated, presumably with the pulled-out biotin−lipid molecules (data not shown). This observation suggests that new molecules are interacting during each binding event.

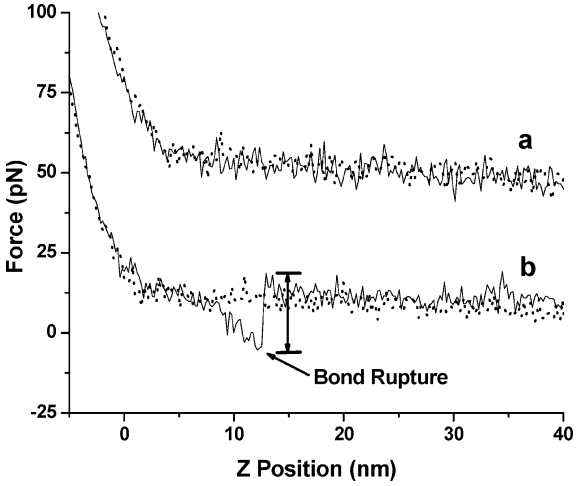


**Figure 3.** Force−distance curves from the measurement involving lipid extraction from a gel-phase DMPC layer at a displacement rate of 10 nm/s. Figure 3a shows an example of a force curve in the absence of bond formation. Figure 3b shows an example of a force curve with bond formation followed by bond rupture. Both the approach (····) and retraction (−−) curves are plotted for each case. Curves are offset for clarity.

## III. Data Analysis

Each measured force curve was analyzed separately via a scripted analysis program written for Labview (National Instruments).[13] Figure 3 shows examples of typical force−distance curves without (Figure 3a) and with (Figure 3b) a bond rupture event. When a rupture event occurred, the measured tip deflection at rupture was multiplied by the spring constant to obtain the rupture force. Force measurements were binned into histograms for each loading rate, showing the percent frequency of events versus the force. The error in rupture force was estimated to range between 7 and 15 pN depending on loading rate. The appropriate bin size of the histograms depends on the error estimated for each particular measurement.[31] Error propagation in this case incorporated both the error in the spring constant and the error due to the tip fluctuations. Lower amounts of noise were found in measurements taken at lower loading rates. Bin sizes from 7 to 10 pN were typical for measurements at lower loading rates ranging from 50 to 650 pN/s, while for faster loading rates (650−6500 pN/s), they were between 10 and 15 pN. Histograms were analyzed by both the DFS method derived by Evans[9,7] and the FM theory of Szabo and Hummer.[10]

**3.1. Dynamic Force Spectroscopy Analysis.** Figure 4a,b illustrates the physical situation modeled by the DFS analysis. Figure 4a shows the situation where one barrier between the bound and the free (dissociated) states is present. In this case, an external force, $F$, creating an external force is applied in the direction of the thermally averaged projection ($x$·cos $\theta$), decreasing the energy barrier by ($F$·cos $\theta$)$x$. This can create a transient capture well, which, if the force applied is great enough, can be deeper than the minimum of the bound state. The energy, $E_b$, required for a bond to move from its bound state to a free state along the potential energy landscape is then lowered by an amount equal to this mechanical energy. This increases the flux of states from the free-energy minimum over the transition barrier to the unbound state, and thereby increases the rate of dissociation.

Figure 4b shows the situation when two energy barriers between the bound and the free states are present. Similar to the case of a single barrier, a mechanical force is applied to the bond, decreasing the energy barrier by ($F$·cos $\theta$)$x$. However in

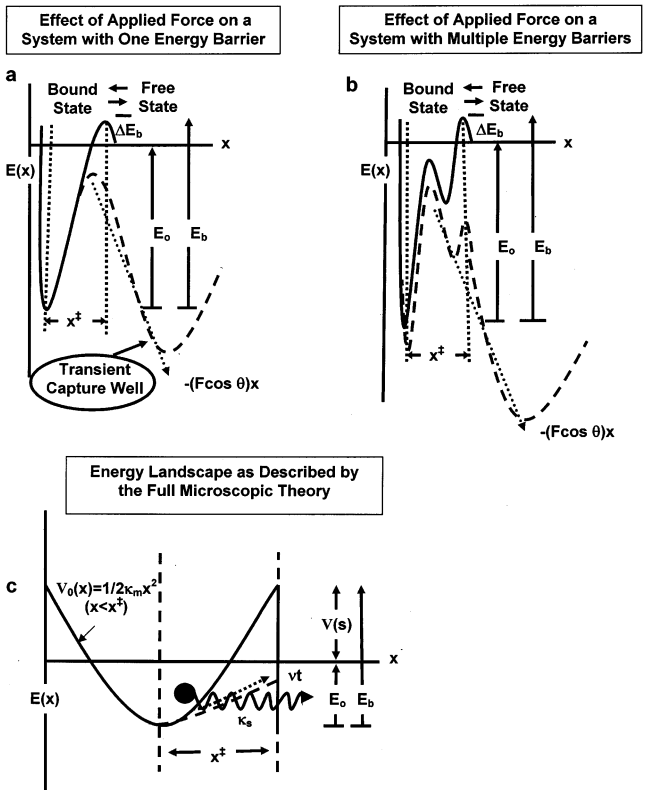


**Figure 4.** Potential energy diagram in the presence of time-dependent force as described by the DFS model. The solid line represents the potential without an external force. The dashed line represents the potential with an applied force. (Figure 4a,b adapted from Evans.[6,7]) Figure 4a shows an energy diagram with only a single barrier, while Figure 4b shows multiple barriers. Figure 4c shows the energy landscape as described by the full microscopic theory. (Figure 4c adapted from Hummer and Szabo.[10]) Parameters in this diagram are as follows: $x^{\ddagger}$ is the distance between the free-energy minimum and the barrier, $\nu$ is the pulling velocity, $t$ is time, $\kappa_m$ is the molecular spring constant, $\kappa_s$ is the harmonic force constant, $E_b$ is the initial height of the energy barrier, $E_o$ is the binding energy, $\Delta E_b$ is the entrance barrier, and $(f \cos \theta)x$ is the mechanical energy applied by an external force, $f$.

this case, the outer energy barrier will typically be manifested in the force curves upon application of lower forces, while the inner energy barrier may be revealed upon application of higher forces.

*3.1.1. DFS − Direct Fit Method.* The equation describing the rate coefficient for the dissociation of a bond in the presence of a time-dependent force, $F(t)$, is given by[1]

$$k(t) = k_0 \exp[\beta F(t) x^{\ddagger}] \tag{1}$$

where $k_0$ is the intrinsic rate constant, $x^{\ddagger}$ is the distance from the free-energy minimum to the transition barrier, and $\beta^{-1} = k_B T$, where $k_B$ is Boltzmann's constant and $T$ is the absolute temperature. When the force $F(t)$ increases linearly with time, such that $\beta F(t) = \kappa_s \upsilon t$ where $\upsilon$ is the pulling velocity and $\kappa_s$ is the harmonic force constant scaled by $k_B T$, the survival probability or the probability that a bond rupture has not occurred before time $t$ is

$$S(t) = \exp\left[-\frac{k_0}{\kappa_s \upsilon x^{\ddagger}}(e^{\kappa_s \upsilon x^{\ddagger} t} - 1)\right] \tag{2}$$

If this result is used, the distribution describing the most probable rupture force, based on the DFS model, is

$$p(F) = \frac{\beta k_0}{\kappa_s \upsilon} \exp\left[\beta F x^{\ddagger} - \frac{k_0}{\kappa_s \upsilon x^{\ddagger}}(e^{(\beta F x^{\ddagger})} - 1)\right] \tag{3}$$

Figure 5 a−d gives examples of histograms of the frequency of rupture as a function of the rupture force for gel- and fluid-phase DMPC. Histograms for each loading rate, $\kappa_s \nu$, were fit to eq 3, to obtain values for $k_0$ and $x^{\ddagger}$. The fit to eq 3 is given by the open circles in Figure 5. We refer to this approach as the "DFS − Direct Fit". Values of $k_0$ and $x^{\ddagger}$ obtained from measurements with fluid-phase DTPC and with fluid-phase DMPC were averaged and are given in Table 1.

However, with gel-phase DMPC, the values of $k_0$ and $x^{\ddagger}$ change in a statistically significant way over the range of loading rates, so that averaging values over the entire range of loading rates was not justified. Instead, values for experiments involving gel-phase DMPC were broken up into two regimes depending on the loading rate. Values for regime 1, which are attributed to an outer energy barrier, are an average of each parameter determined at loading rates between 50 and 650 pN/s. Values for regime 2 (inner energy barrier) are the average parameter values for loading rates between 650 and 6500 pN/s. Averaged values within these two regimes are also given in Table 1 under the "DFS − Direct Fit" heading.

*3.1.2. DFS − Most Probable Force Method.* An alternative method of determining $x^{\ddagger}$ and $k_0$ on the basis of the DFS model involves constructing plots of the most probable force $F_m$ versus the logarithm of the loading rate. $F_m$ is the maximum of $p(F)$ obtained in the fit of eq 3 to the histograms of the frequency of the rupture event as a function of rupture force. Figure 6a gives plots of $F_m$ as a function of $\ln(\kappa_s \nu)$ for both fluid- and gel-phase DMPC. According to the DFS theory, these plots are related to $x^{\ddagger}$ and $k_0$ by the following expression

$$F_m = (k_B T / x^{\ddagger}) \ln\left(\frac{\kappa_s \nu x^{\ddagger}}{k_0 k_B T}\right) \tag{4}$$

Thus, the slope of $F_m$ versus $\ln(\kappa_s \nu)$ gives $k_B T / x^{\ddagger}$, which can be solved for $x^{\ddagger}$. Extrapolating the $F_m$ versus $\ln(\kappa_s \nu)$ plot to $F_m = 0$ gives an expression for $k_0$

$$k_0 = \kappa_s \upsilon_{F_m=0} x^{\ddagger} / (k_B T) \tag{5}$$

where $\kappa_s \upsilon_{F_m=0}$ is the loading rate at zero force. We refer to this method of data analysis as the "DFS − Most Probable Force" method. The parameters for $k_0$ and $x^{\ddagger}$ thus determined are given in Table 1.

From values of $k_0$ obtained using either the DFS direct fit or the DFS most probable force method, an additional parameter can be obtained. The difference between the energy minimum of the ground state and the initial energy barrier $E_b$ is obtained from

$$k_0 = 1/t_D \exp(-E_b / k_B T) \tag{6}$$

where $t_D$ is the diffusive relaxation time and is assumed to be $10^{-9}$ s. Finally, we calculate a thermal activation force, $f^{\ddagger} = k_B T / x^{\ddagger}$. Values of $E_b$ and $f^{\ddagger}$ are reported in Table 1.

**3.2. Analysis Using the Full Microscopic Theory.** Figure 4c shows a potential energy diagram modeled by FMT.[10] FMT depicts a system in which the bond diffuses on a harmonic free-energy surface described by $V_0(x) = {}^1/_2 k_B T \kappa_m x^2$ where $\kappa_m$ is the molecular spring constant. The surface has a sharp cusp at $x = x^{\ddagger}$, and at $x > x^{\ddagger}$, the bond is ruptured. Application of a force by pulling on this molecular spring with velocity $\nu$ adds

**TABLE 1: Calculated Parameters Describing the Energy Landscape for Lipid Pullout Determined from Dynamic Force Spectroscopy and Full Microscopic Methods Using Both Most Probable and Average Forces[a]**

Dynamic Force Spectroscopy (DFS) − Direct Fit

| lipid | $x^{\ddagger}$ (nm) | $k_0$ (sec$^{-1}$) | $E_b$ (KT) | $f^{\ddagger}$(pN) |
|---|---|---|---|---|
| fluid DTPC | 0.5 ± 0.2 | 1.0 ± 0.6 | 20.7 ± 0.6 | 10 ± 4 |
| fluid DMPC | 0.6 ± 0.3 | 0.8 ± 0.8 | 21 ± 1 | 9 ± 3 |
| gel DMPC (outer) | 0.46 ± 0.07 | 0.2 ± 0.2 | 22 ± 1 | 9 ± 2 |
| gel DMPC (inner) | 0.18 ± 0.02 | 1.1 ± 0.6 | 21 ± 1 | 26 ± 4 |

Dynamic Force Spectroscopy − Most Probable Force

| lipid | $x^{\ddagger}$ (nm) | $k_0$ (sec$^{-1}$) | $E_b$ (KT) | $f^{\ddagger}$ (pN) |
|---|---|---|---|---|
| fluid DTPC | 0.30 ± 0.04 | 1.4 ± 0.3 | 20 ± 2 | 14 ± 3 |
| fluid DMPC | 0.37 ± 0.07 | 1.5 ± 0.2 | 23 ± 2 | 11 ± 2 |
| gel DMPC (outer) | 0.4 ± 0.1 | 0.24 ± 0.1 | 22 ± 4 | 11 ± 3 |
| gel DMPC (inner) | 0.06 ± 0.006 | 3.4 ± 0.4 | 20 ± 1 | 65 ± 6 |

Full Microscopic Theory (FMT) − Direct Fit

| lipid | $x^{\ddagger}$ (nm) | $k_0$ (sec$^{-1}$) | $\kappa_m$ (pN/nm) | $f^{\ddagger}$ (pN) |
|---|---|---|---|---|
| fluid DTPC | 0.6 ± 0.2 | 0.3 ± 1 | 219 ± 128 | 8 ± 4 |
| fluid DMPC | 0.5 ± 0.1 | 0.4 ± 0.8 | 182 ± 73 | 9 ± 3 |
| gel DMPC | 0.38 ± 0.2 | 0.4 ± 0.9 | 451 ± 253 | 14 ± 5 |

Full Microscopic Theory − Average Force

| lipid | $x^{\ddagger}$ (nm) | $k_0$ (sec$^{-1}$) | $\kappa_m$ (pN/nm) | $f^{\ddagger}$ (pN) |
|---|---|---|---|---|
| fluid DTPC | 0.49 ± 0.01 | 0.16 ± 0.03 | 90 ± 7 | 8.4 ± 0.2 |
| fluid DMPC | 0.51 ± 0.01 | 0.18 ± 0.03 | 99 ± 23 | 8.1 ± 0.2 |
| gel DMPC | 0.14 ± 0.004 | 1.5 ± 0.2 | 425 ± 36 | 29.4 ± 0.8 |

[a] Values in parentheses describe coefficients found for gel-phase DMPC lipid extraction at high loading rates (700−6500 pN/S).

a new potential $V_s$ to the energy landscape where $V_s = {}^1/_2 k_B T \kappa_s (x - vt)$. Here, $\kappa_s$ is the effective force constant of the cantilever and linker. $V_s$ lowers the barrier to rupture. This theory only considers the escape from a well confined by a single barrier. The barrier shape in this case is sharp and cusp-like, which is suggested to approximate the snapping motion of the tip during bond rupture. Like the DFS theory, FMT is used to obtain parameters such as the distance from the energy minimum to the energy barrier, $x^{\ddagger}$, and the dissociation rate constant $k_0$. An extra parameter, the molecular spring constant, $\kappa_m$, is incorporated into the overall spring constant, $\kappa$, where $\kappa = \kappa_m + \kappa_s$.

*3.2.1. FMT − Direct Fit.* The histograms for each loading rate were also analyzed using FMT.[10] In this method, the probability distribution for bond rupture $p(F)$ is given as follows:

$$p(F) = (\kappa_s v)^{-1}[-S(t^*)\,dt^*]_{t^*=(\beta F+\kappa_s x^{\ddagger})/\kappa_s v} \quad (7)$$

where $S(t)$ for this equation is

$$S(t) = \exp\left[-\frac{k_0 e^{-\kappa_s (x^{\ddagger})^2/2}}{\kappa_s v x^{\ddagger}(\kappa_m/\kappa)^{3/2}}(e^{\kappa_s v x^{\ddagger} t-(\kappa_s v t)^2/(2\kappa)} - 1)\right] \quad (8)$$

Here, $\kappa_m$ is the molecular spring constant. Substituting eq 8 into eq 7 gives

$$p(F) = (\kappa_s v)^{-1} \exp\left[-(\kappa_s t^* v)^2/(2\kappa) + \kappa_s t^* v - \kappa_s (x^{\ddagger})^2/2 - \left(\frac{e^{-\kappa_s (x)^2/2}(e^{\kappa_s t^* x^{\ddagger} v-(\kappa_s t^* v)^2/(2\kappa)} - 1)}{(\kappa_m/\kappa)^{3/2}\kappa_s x^{\ddagger} v}\right)\right]\left(\frac{k_0(\kappa_s x^{\ddagger} v - (\kappa_s v)^2 t^*/\kappa)}{(\kappa_m/\kappa)^{3/2}\kappa_s x^{\ddagger} v}\right) \quad (9)$$

A nonlinear least-squares fit of eq 9 to the histograms for each loading rate was performed using *Igor Pro 4* software (WaveMetrics, Inc.), to obtain the best-fit parameters for $\kappa_m$, $k_0$, and $x^{\ddagger}$ at each loading rate. We refer to this approach as the "FMT − Direct Fit" (Table 1). Representative histograms and data fits are shown in Figure 5a−d (solid line). In this case, the parameters appear to vary over the range of loading rates. However, both the student's *t*-test for comparison of means and a one-way analysis of variance showed that there are no statistically significant differences in the $k_0$ values obtained from the FMT − direct fit compared to experimental data obtained with gel-phase DMPC over the range of loading rates used. They are therefore taken to be constant over the range of loading rates. This result is supported by additional analyses described in the text to follow.

*3.2.2. FMT − Average Fit.* Szabo and Hummer[10] showed that $k_0$ and $x^{\ddagger}$ could also be readily obtained from the dependence of the average rupture force on the loading rate. The average rupture force was calculated for each loading rate directly from the data (Figure 6b). In this case, some data sets contained a few outlying rupture forces, which were two to three times that of the most probable force. These outliers are attributed to the infrequent occurrence of multiple binding events. Because the theory only describes single-bond rupture events, these outlying data were ignored when calculating the average force $F$. The plot of the average force versus the log of the loading rate (Figure 6b) was then fit using eq 10

$$\beta\bar{F} = -\kappa_s[x^{\ddagger} - v\int_0^{\tau} S(t)\,dt] \quad (10)$$

Numerical integration of this equation was performed using the trapezoid rule with the rupture lifetime $\tau = x(t)\kappa/\kappa_s v$ at long times and $\tau = \sqrt{x(t)\kappa/v\kappa_s}$ at short times.[10] The best fit was then obtained for each experimental case. Error values for each fitting parameter were obtained by calculating the amount each parameter was allowed to deviate from the best fit and still fall within a designated range of the variance of the fit, $\chi^2$. In this case, the $\chi^2$ range was ±10% of the $\chi^2$ obtained from the best fit. The fitted parameters are given in Table 1.

**3.3. Sensitivity of Fit.** In multiple fits, we found that, while the $x^{\ddagger}$(and $f^{\ddagger}$) value was obtained with relatively small error, this was not the case for $k_0$ (and $E_b$) and $\kappa_m$. The origin of the relatively large error in these rate-constant-dependent parameters arises because $k_0$ is a prefactor to an exponential function. Large changes in $k_0$ produce relatively small changes in the fit. A better determination of $k_0$ would require less error in the initial histograms shown in Figure 5, a level of precision that apparently is not available with our technology.

## IV. Results

**4.1. DFS − Direct Fit and FMT − Direct Fit Methods.** Figure 5 shows representative force histograms for both the fluid- and gel-phase DMPC monolayer. Loading rates are shown for both fluid and gel states at ca. 120 pN/s and 1500 pN/s, which correspond to slow and fast loading rates, respectively. The fits were obtained with both the DFS − direct fit (eq 3; Figure 5a−d, open circles) and the FMT − direct fit (eq 9; Figure 5a−d, line) analysis methods. A noticeable feature in these plots is the increase in both the magnitude of the most probable rupture force, $F_m$, and the width of the histogram as a function of loading rate. The increase in $F_m$ with increased loading rate is greater for the gel-phase DMPC layer relative to the fluid-phase. This increase is manifested in parameters shown in Table 1. For example, the $x^{\ddagger}$ value obtained in the DFS − direct fit for the fluid-phase DMPC layer is nearly a factor of

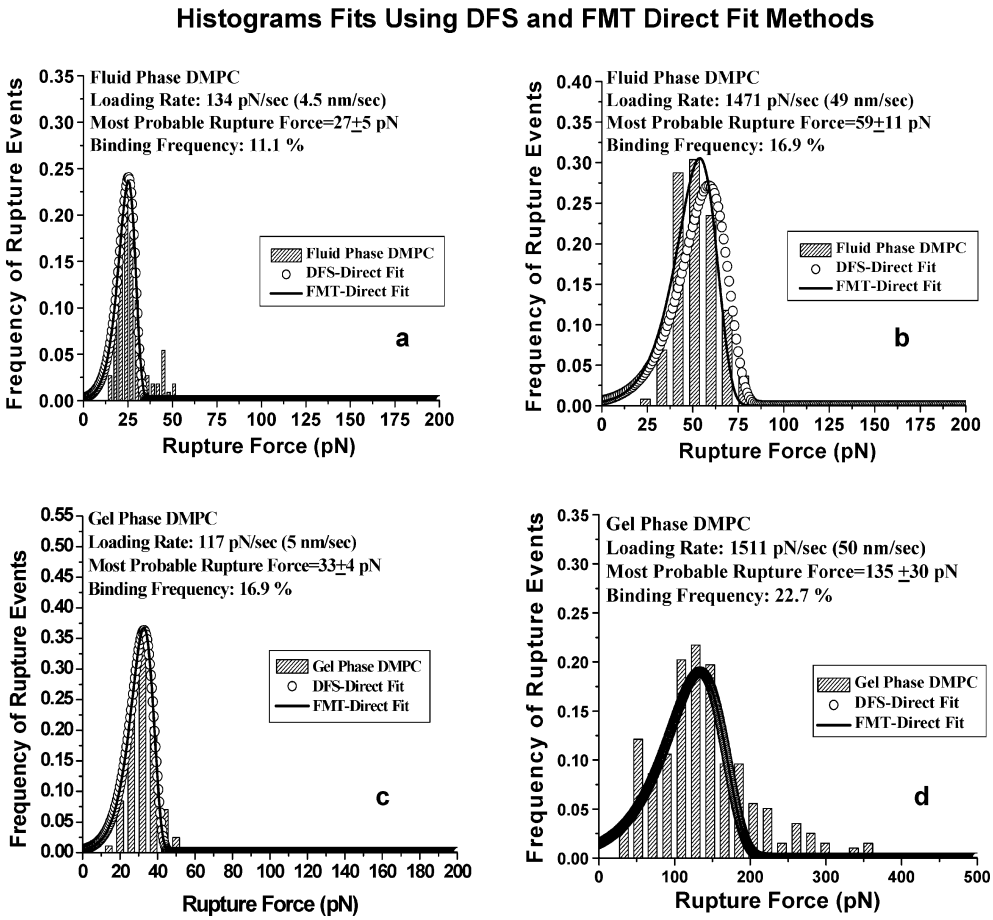


**Figure 5.** Force histograms obtained with both fluid- and gel-phase DMPC. A comparison of pulling rates at approximately 5 and 50 nm/s is given. The data are fit by both the dynamic force spectroscopy−direct fit (open circles) and the full microscopic theory−direct fit (solid line) methods.

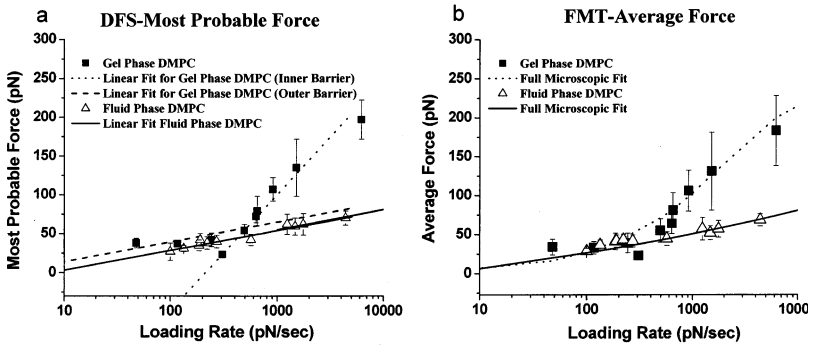


**Figure 6.** Dynamic force spectrum of lipid pullout and fits to the data obtained with the (a) DFS − most probable force method and the (b) FMT − average force method. Plots include both experimental data and best-fit lines for gel-phase DMPC (■) and fluid-phase DMPC (△).

3 greater than $x^{\ddagger}$ obtained for the inner barrier in the gel-phase DMPC layer. This increase in $x^{\ddagger}$ is found to be somewhat less in the FMT − direct fit analysis where the increase in $x^{\ddagger}$ is only about a factor of 1.5.

**4.2. DFS − Most Probable Force Method.** We also analyzed the data shown in Figure 5 using the DFS − most probable force method. Figure 6a shows the dynamic force spectra for both fluid- and gel-phase lipid layers with the fits obtained using the DFS − most probable force analysis. The figure shows that, at slow loading rates, $F_m$ is the same, within error, for both fluid and gel phases. However, at loading rates $\kappa_s\nu > 650$ pN/s, the anchoring strength of DMPC in the gel phase increases much more rapidly with loading rate than for fluid DMPC.According to the theory, the two slopes found for gel-phase DMPC indicate that two barrier crossings govern lipid pullout. These two barriers, which we refer to as the inner and outer barriers, predominate at slow and fast loading rates, respectively, as in the schematic shown in Figure 4b. On the other hand, the data obtained with fluid-phase DMPC over the same range of loading rates exhibit a single slope, suggesting that only one barrier is required to model lipid extraction from the fluid phase. The slopes of the line, obtained from weighted linear least-squares fits to the data in Figure 6a, are similar for the fluid phase and the slow loading regime with the gel phase, while the slope of the line that fits the gel-phase data obtained at high loading rates ($\kappa_s\nu > 650$ pN/s) increases by nearly a factor of 5 relative to the low-loading-rate fit. This suggests that it takes more work to pull the lipid from the gel-phase monolayer relative to fluid.

Table 1 gives parameters obtained by analyzing the linear

regions of the plots in Figure 6a. The distances to the transition state, $x^{\ddagger}$'s, obtained with fluid-phase DMPC and with gel-phase DMPC at slow loading rates are $0.4 \pm 0.1$ and $0.06 \pm 0.006$ nm, respectively. The dissociation rates, $k_0$'s, obtained with the fluid- and gel-phase DMPC in this loading regime are, respectively, $0.24 \pm 0.1$ s$^{-1}$ and $3.44 \pm 0.4$ s$^{-1}$, suggesting a significant change in the lipid pullout dissociation rate upon phase transition. Finally, the values of the energy barriers, $E_b$'s, to extract the lipids are essentially the same across all of the measurements described, although the standard deviations vary significantly. Data analyzed using the DFS − direct fit approach gave results which are similar to those obtained using the DFS − most probable force approach and can be compared in Table 1.

**4.3. FMT − Average Force Method.** Figure 6b shows a dynamic force spectrum obtained using the FMT − average force approach. Within the range of experimental error, the data for both fluid- and gel-phase lipids are described by eq 10 throughout the range of loading rates examined in these measurements. Interestingly, the FMT − average force method also reveals a discontinuity in the average force to remove the gel-phase lipid at higher loading rates. Fitting eq 10 to the points in Figure 6 gives the fits shown by the lines in the figure. From the fits, parameters are extracted and reported in Table 1 (FMT − Average Force).

Similar to parameters obtained with the DFS − most probable force method, these calculated $x^{\ddagger}$ values are $0.14 \pm 0.004$ and $0.51 \pm 0.01$ nm for the gel- and fluid-phase lipids, respectively. The $k_0$ value is also greater in the gel phase relative to the fluid phase. Finally, the fit to FMT makes use of another parameter, $\kappa_m$, which is the molecular spring constant. Table 1 shows that this parameter is four times larger in the gel phase relative to the fluid phase.

**4.4. DTPC.** To determine whether the trends reported here reflect differences in the lipid phase state, we also obtained lipid extraction data with a fluid-phase DTPC layer. DTPC and DMPC share the same headgroups, but the former has one less carbon in the hydrocarbon tails. Table 1 also gives parameters obtained with the four analytical approaches described here, but with a fluid DTPC monolayer. As expected, the fluid-phase DTPC parameters are quite similar to those obtained with fluid-phase DMPC.

## V. Discussion

The results and analysis presented here provide insight into the forces experienced by a lipid when it is removed from its equilibrium position within a lipid layer. These data show directly that it is more difficult to extract the lipid when the lipid is in the gel phase relative to fluid. We also obtain parameters that quantify this process and analyze them in terms of what is known about packing in phospholipid bilayers.

The analysis of the force data provides some absolute numbers regarding the energy landscape governing forced lipid extraction from a lipid layer. From Table 1, we find values for $x^{\ddagger}$ from fluid-phase pulling measurements of between 3 and 6 Å, which are clearly molecular dimensions. The determined values for $k_0$ are on the order of $0.16-1.5$ s$^{-1}$ albeit with fairly large error bars, as discussed already. The $\kappa_m$ values for the different systems further indicate that the molecular spring constant is stiffer for gel-phase relative to the fluid-phase lipids, consistent with intuition.

There have been a number of previous determinations of parameters similar to those obtained here. For example, Evans used BFP to examine lipid pullout from an SOPC bilayer. SOPC differs from the DMPC used here in that SOPC has two 18-carbon alkane chains, one of which contains a double bond. Analysis of the BFP measurement for fluid-phase SOPC using the DFS (most probable force) approach revealed the presence of two energy barriers, or equivalently, two values of $x^{\ddagger}$. The inner barrier gave a bond rupture distance of 0.7 nm, and the outer barrier gave a bond rupture distance of 1.2 nm. The outer energy barrier was explained as the distance it takes to pull the lipid completely from the layer, while the inner energy barrier was explained as coinciding with the position of the double bond in the unsaturated hydrocarbon region of the lipid.[8] Interestingly, our measurements with fluid-phase DMPC were fitted using only one barrier, although the AFM measurements do not span as wide a dynamic loading range as the BFP measurements. The $k_0$ values for the inner and outer barriers for SOPC lipid extraction were 0.9 and 0.09 s$^{-1}$, respectively. Our values for $k_0$ vary from 0.18 to 1.5 s$^{-1}$ for fluid-phase DMPC.

Values for both $x^{\ddagger}$ and $k_0$ have been determined in a number of other biologically relevant systems ranging from the L-selectin and P-selectin interaction with their natural ligand (P-selectin glycoprotein ligand-1),[29] the unfolding of the Ig27 domain of titin,[4] the biotin−steptavidin interaction,[6,33] the $\alpha_5\beta_1$ integrin−fibronectin interaction,[15] the fibronectin−surface interaction,[24] and the unzipping of DNA.[14] In most of these determinations, the $x^{\ddagger}$ values were between 0.02 and 0.9 nm, with the majority in the 0.2−0.6 nm range. In some cases where two barriers were observed, somewhat higher values for this parameter were obtained, ranging up to 3.6 nm in the integrin−fibronectin study.[15] Our determined values of $x^{\ddagger}$ easily fall within the first group of parameters and again emphasize their molecular origin. Specifically, the $x^{\ddagger}$ values strongly indicate that the barrier to lipid removal does not comprise elongation of the entire chain, but rather the movement around a few molecular-scale interactions.

If there is general agreement in determinations of $x^{\ddagger}$ values among the different systems examined already, this is not the case for $k_0$ values. The values of $k_0$ determined in other systems ranged from ca. $10^{-6}$ to $10^{-3}$ s$^{-1}$ for the streptavidin−biotin bond,[33] while somewhat weaker interactions gave $k_0$ values from 0.1 to ca. 10 s$^{-1}$. Our $k_0$ values of 0.16 to 3.4 s$^{-1}$ fall in this latter category, which suggests that the activation barrier to lipid extraction is lower than might be expected intuitively.

With regard to differences between gel- and fluid-phase lipids, Figure 5 shows that there is a definite difference in the force required to extract a lipid between the gel and fluid phases at high loading rates. At a loading rate of 50 nm/s (1500 pN/s), the anchorage force for the gel-phase DMPC is $131 \pm 37$ pN as opposed to $59 \pm 11$ pN for the fluid-phase. To get a more descriptive picture, the dynamic force spectrum (Figure 6) of the gel versus fluid data shows clearly a much steeper slope of the line fitting the gel-phase data compared to fluid over the given range of loading rates. As shown already, this steeper slope corresponds to a smaller value for $x^{\ddagger}$, the distance by which the lipid must be moved in order to remove it. $x^{\ddagger}$ is related to the thermal activation force $f^{\ddagger}$ through $f^{\ddagger} = k_B T/x^{\ddagger}$. This implies that the steeper slope observed in the high-loading-rate gel-phase measurements corresponds to a greater thermal activation force. Our analysis showed that $x^{\ddagger}$ was ca. 2−4 times smaller in the gel versus fluid measurement, which implies that $f^{\ddagger}$ is ca. 2−4 times larger in the gel phase relative to fluid. The compact nature of the gel-phase lipid prevents removal of the lipid from the membrane with the same force required for a

**TABLE 2: Comparison of the Gel- vs Fluid-Phase DMPC Membrane Characteristics**[3,12,18,21,25,26,28,32,34]

| membrane properties | fluid-phase DMPC | gel-phase DMPC |
|---|---|---|
| membrane organization | disordered layer | packed, ordered layer |
| lipid area/molecule | $61.3 \pm 1.2$ Å$^2$ | $47.2 \pm 0.5$ Å$^2$ |
| bond type observed | 4−7 gauche bonds/carbon chain | Aall trans bonds |
| bilayer thickness | 35.1 Å | 41.9 Å |
| tilt angle | 35° | 32° |
| compressibility modulus | $140 \pm 10$ dyn/cm | $320 \pm 25$ dyn/cm |
| lipid mobility | increased mobility | decreased mobility |
| bond motion | rotational motion around headgroups | restricted bond motions (no C−C bond rotation) |
| lateral diffusion | $10^{-8}$−$10^{-10}$ cm$^2$/s | $10^{-10}$−$10^{-11}$ cm$^2$/s |

mobile, less compact fluid phase. At the same time, $k_0$ values were found to be somewhat larger in the gel phase relative to fluid.

Analyses performed by the DFS − most probable fit method shows the presence of two energy barriers for the gel-phase lipid layer. One occurs at loading rates of <650 pN/s and is of the same order as that found for the one barrier exhibited by the fluid-phase lipid system. The second, observed at higher loading rates, gives a $f^{\ddagger}$ some six times larger than that found for either the fluid phase or the outer barrier for the gel phase. The origin of this inner barrier must lie in the details of the gel-phase chain interactions, but cannot be discerned in the present study.

We have previously used SFA measurements to examine differences between extraction force between lipid bilayers in the fluid and gel phases. The lipid examined in the latter case was also biotinylated DPPE, embedded in a dilaurylphosphatidylethanolamine (DLPE) matrix. In contrast to the results presented here, a sixfold *increase* in the intermembrane adhesion was observed for fluid-phase relative to gel-phase lipid layers. This increase was attributed to the increased mobility present in the fluid phase relative to the gel phase. Increased mobility allows more intermembrane bonds to form, and results in increased adhesion. The SFA measurements determine the adhesion energy measured under near-equilibrium conditions and averaged over an area, as opposed to the force required for the rupture of a single bond measured under far-from-equilibrium conditions. In the SFA measurements, the force profiles measured again directly after surface separation exhibited substantial changes in the force−distance curves and a signficant decrease in adhesion. The latter findings indicated that there was a cohesive failure of the bilayer and that the streptavidin−biotin bond is therefore stronger than the lipid anchorage.[17]

In the gel phase, all lipid molecules are in an extended configuration with the hydrocarbon region consisting of all trans bonds.[3,12,32,34] This allows for tight packing of the molecules. In the fluid phase, there are approximately 4−7 gauche bonds per carbon chain.[18,25,28] This leads to more disorder within the liquid-crystalline layer with extensive rotational motion of the headgroup and individual C−C bonds in the alkyl chain.[21,26] The gel phase of DMPC is 21% denser than the fluid phase. The increase in density clearly changes the barrier required to pull out a lipid. Table 2 gives a short summary of the structural differences between gel- and fluid-phase DMPC lipid membranes.

Also seen in Table 1 is a difference in the values for the distance between the free-energy minimum and the transition barrier, $x^{\ddagger}$. In this case, the $x^{\ddagger}$ value for gel-phase lipids is approximately 2.5−4.5 times larger for the fluid phase than the gel phase. To conclude that the pullout force is due to the extraction of the full hydrocarbon chain of the lipid from the layer would be unreasonable, given that the thickness of the lipid monolayer is much larger than these measured values for $x^{\ddagger}$. The thickness of a DMPC monolayer in the gel phase is 22 Å compared to the 19-Å thickness of a fluid-phase DMPC monolayer.[13] Both values are much larger than those determined for $x^{\ddagger}$; namely, 1 and 5 Å for gel- and fluid-phase lipids, respectively.

## Summary

We show that the force to remove a lipid from a lipid bilayer depends on the phase state of the lipid, with larger pullout forces required when the bilayer is in its gel phase relative to the fluid phase. Through analysis of the force data, we also show that the barrier to lipid removal does not comprise elongation of the entire chain, but rather the movement around a few molecular-scale interactions. We also show the robustness of our data by obtaining comparable data when testing a lipid of similar structure and phase state.

**Acknowledgment.** This work was supported in part by NIH RO1 GM63536 and by the U.S. Department of Energy, Division of Materials Science, under award no. DEFG02-91ER45439 through the Frederick Seitz Materials Research Laboratory at the University of Illinois at Urbana-Champaign

## References and Notes

(1) Bell, I. G. *Science* **1978**, *200*, 618−627.
(2) Brown, D. A. *Trends Cell Biol.* **1992**, *2*, 338−343.
(3) Bueldt, G.; Gally, H. U.; Seelig, J.; Zaccai, G. *J. Mol. Biol.* **1979**, *134*, 673−691.
(4) Carrion-Vazquez, M.; Oberhauser, A. F.; Fowler, S. B.; Marszalek, P. E.; Broedel, S. E.; Clarke, J.; Fernandez, J. M. *Proc. Natl. Acad. Sci. U.S.A.* **1999**, *96*, 3694−3699.
(5) Cevc, G.; Marsh, D. *Phospholipid Bilayers: Physical Principles and Models*; John Wiley & Sons: New York, 1987; Vol. 5.
(6) Evans, E. *Faraday Discuss.* **1998**, *111*, 1−16.
(7) Evans, E. *Annu. Rev. Biophys. Struct.* **2001**, *30*, 105−128.
(8) Evans, E.; Ludwig, F. *J. Phys.: Condes. Matter* **2000**, *12*, A135-A320.
(9) Evans, E.; Ritchie, K. *Biophys. J.* **1997**, *72*, 1541−1555.
(10) Hummer, G.; Szabo, A. *Biophys. J.* **2003**, *85*, 5−15.
(11) Hutter, J. L.; Bechhoefer, J. *Rev. of Sci. Instrum.* **1993**, *64*, 1863−1873.
(12) Janiak, M. J.; Small, D. M.; Shipley, G. G. *Biochemistry* **1976**, *15*, 5, 4575−4580.
(13) Kang, M.; Gewirth, A. A. *J. Phys. Chem. B* **2002**, *106*, 12211−12220.
(14) Koch, S. J.; Wang, M. D. *Phys. Rev. Lett.* **2003**, *91*, 028103.
(15) Kokkoli, E.; Ochsenhirt, S. E.; Tirrell, M. *Langmuir* **2004**, *20*, 2397−2404.
(16) Kuhl, T. L.; Leckband, D. E.; Lasic, D. D.; Israelachvili, J. N. *Biophys. J.* **1994**, *66*, 1479−1488.
(17) Leckband, D. E.; Schmitt, F. J.; Israelachvili, J. N.; Knoll, W. *Biochemistry* **1994**, *33*, 4611−4624.
(18) Levin, I. W.; Bush, S. F. *Biochim. Biophys. Acta* **1981**, *640*, 760−766.
(19) Marra, J.; Israelachvili, J. *Biochemistry* **1985**, *24*, 4608−4618.
(20) Marrink, S.-J.; Berger, O.; Tieleman, P.; Jahnig, F. *Biophys. J.* **1998**, *74*, 931−943.
(21) Marsh, D. *Biochemistry* **1980**, *19*, 1632−1637.
(22) Marsh, D. *CRC Hand Book of Lipid Bilayers*; CRC Press: Boca Raton, FL, 1990.

(23) McConville, M. J.; Menon, A. K. *Mol. Membr. Biol.* **2000**, *17*, 1−16.
(24) Meadows, P. Y.; Bemis, J. E.; Walker, G. C. *Langmuir* **2003**, *19*, 9566−9572.
(25) Nagle, J. F.; Tristam-Nagle, S. *Biochim. Biophys. Acta* **2000**, *1469*, 159−195.
(26) Needham, D.; Evans, E. *Biochemistry* **1988**, *27*, 8261−8269.
(27) Nelson, D. L.; Cox, M. M. *Lehninger Principles of Biochemistry*, 3rd ed.; Worth Publishers: New York, 2000.
(28) Pink, D. A.; Green, T. J.; Chapman, D. *Biochemistry* **1980**, *19*, 349−56.
(29) Rinko, L. J.; Lawrence, M. B.; Guilford, W. H. *Biophys. J.* **2004**, *86*, 544−554.
(30) Sivasankar, S.; Brieher, W.; Lavrik, N.; Gumbiner, B.; Leckband, D. *PNAS* **1999**, *96*, 11820−11824.
(31) Taylor, J. R. *An Introduction to Error Analysis: The Study of Uncertainties in Physical Measurements*; University Science Books: Mill Valley, CA, 1982.
(32) Tristram-Nagle, S.; Liu, Y.; Legleiter, J.; Nagle, J. *Biophys. J.* **2002**, *83*, 3324−3335.
(33) Yuan, C.; Chen, A.; Kolb, P.; Moy, V. T. *Biochemistry* **2000**, *39*, 10219−10223.
(34) Zubrzycki, I.; Xu, Y.; Madrid, M.; Tang, P. *J. Chem. Phys.* **2000**, *112*, 3437−3441.